

# High-pressure / High-temperature Studies on the Stannides $RENiSn$ ( $RE = Ce, Pr, Nd, Sm$ ) and $REPdSn$ ( $RE = La, Pr, Nd$ )

Jan F. Riecken<sup>a</sup>, Gunter Heymann<sup>b</sup>, Wilfried Hermes<sup>a</sup>, Ute Ch. Rodewald<sup>a</sup>, Rolf-Dieter Hoffmann<sup>a</sup>, Hubert Huppertz<sup>b</sup>, and Rainer Pöttgen<sup>a</sup>

<sup>a</sup> Institut für Anorganische und Analytische Chemie, Universität Münster, Corrensstraße 30, D-48149 Münster, Germany

<sup>b</sup> Institut für Allgemeine, Anorganische und Theoretische Chemie, Leopold-Franzens-Universität Innsbruck, Innrain 52a, A-6020 Innsbruck, Austria

Reprint requests to R. Pöttgen. E-mail: pottgen@uni-muenster.de

*Z. Naturforsch.* **2008**, *63b*, 695–706; received March 5, 2008

*Dedicated to Professor Gérard Demazeau on the occasion of his 65<sup>th</sup> birthday*

The normal-pressure (NP) orthorhombic  $TiNiSi$ -type (space group  $Pnma$ ) stannides  $RENiSn$  ( $RE = Ce, Pr, Nd, Sm$ ) and  $REPdSn$  ( $RE = La, Pr, Nd$ ) were transformed into the corresponding hexagonal  $ZrNiAl$ -type (space group  $P62m$ ) high-pressure (HP) modifications under multianvil high-pressure (7.5–11.5 GPa) high-temperature (1100–1200 °C) conditions. The structures of NP-CeNiSn, HP-PrNiSn, NP-NdNiSn, HP-LaPdSn, HP-PrPdSn, and HP-NdPdSn were refined from single crystal X-ray diffractometer data. Structural data for HP-SmNiSn were obtained from a Rietveld powder refinement. The high-pressure phase transition significantly changes the rare earth coordination, *i. e.* 4  $RE + 6 Ni(Pd) + 6 Sn$  atoms for the NP-phases and 6  $RE + 5 Ni(Pd) + 6 Sn$  atoms for the HP-phases. Susceptibility measurements of HP-PrPdSn and HP-NdPdSn reveal paramagnetic behavior with experimental magnetic moments of 3.61(1)  $\mu_B/Pr$  atom and 3.66(1)  $\mu_B/Nd$  atom, respectively. Low-temperature susceptibility and specific heat data point to inhomogeneous magnetism and spin-glass behavior, respectively.

**Key words:** Intermetallics, High Pressure, Magnetism, Crystal Chemistry

## Introduction

Equiatomic rare earth ( $RE$ )-transition metal ( $T$ )- $X$  ( $X =$  element of the 3<sup>rd</sup>, 4<sup>th</sup>, or 5<sup>th</sup> main group) compounds have intensively been investigated in the last forty years with respect to their greatly varying magnetic and electrical properties. These compounds crystallize with more than 30 different structure types [1–3], most of them derived from the aristotype  $A1B_2$  [4]. In several series  $RETX$ , the structure type changes as a function of the size of the rare earth element (lanthanide contraction). Often, for one or two of the  $RETX$  compounds close to the switch in structure type, one observes temperature driven dimorphism. Prominent examples are the low- (LT) and high-temperature (HT) modifications of  $HoAuSn$  [5],  $ErAuSn$  [6],  $ErPdSn$  and  $TmPdSn$  [7],  $TmAgSn$  [8],  $LuAgSn$  [9], or  $CePdAl$  [10].

The transition from the high- into the low-temperature phase can be realized for the slightly

larger rare earth elements by simultaneously applying high-pressure (HP) and high-temperature (HT). This was recently demonstrated for the stannides  $REPtSn$  ( $RE = La-Nd, Sm$ ) [11–13],  $CePdSn$  [14], and  $ErAgSn$  [15]. The phase transition drastically changes the local coordination of the rare earth element and thus strongly influences the magnetic ground state. To give an example, the magnetic ordering temperature of the normal-pressure (NP) phases of  $CePdSn$  ( $T_N = 7.5$  K) [16] and  $CePtSn$  ( $T_N = 8$  K) [11, and refs. therein] drop to  $T_N = 5$  and 2.1 K for HP- $CePdSn$  [14] and HP- $CePtSn$  [17], respectively.

We have extended these high-pressure/high-temperature investigations with respect to the  $RENiSn$  and  $REPdSn$  series. While the  $RENiSn$  stannides [18] crystallize all with the orthorhombic  $TiNiSi$  type [19], the  $REPdSn$  stannides [7, 18] show a switch in the structure type.  $ErPdSn$ ,  $TmPdSn$  [7], and  $YbPdSn$  [20, 21] have a  $ZrNiAl$ -type [22, and refs. therein] low-temperature modification. Herein, we report on high-

Table 1. Experimental details of the high-pressure/high-temperature experiments for the *RETSn* ( $RE = \text{La, Pr, Nd, Sm}$ ;  $T = \text{Ni, Pd}$ ) samples.

Sample	Max. pressure	Temperature program
HP-CeNiSn	7.5 GPa	↗1150 °C/15 min, →1150 °C/15 min, ↓800 °C/1 min, ↘800 to 700 °C/210 min, ↓r. t.
HP-PrNiSn	11.5 GPa	↗1100 °C/20 min, →1100 °C/5 min, ↓800 °C/1 min, →800 to 700 °C/60 min, ↓r. t.
HP-NdNiSn	11.5 GPa	↗1100 °C/20 min, →1100 °C/5 min, ↓800 °C/1 min, →800 to 700 °C/60 min, ↓r. t.
HP-SmNiSn	10.5 GPa	↗1150 °C/20 min, →1150 °C/10 min, ↓900 °C/1 min, ↘900 to 700 °C/180 min, ↓r. t.
HP-LaPdSn	10.5 GPa	↗1200 °C/20 min, →1200 °C/5 min, ↓750 °C/1 min, ↘750 to 500 °C/180 min, ↓r. t.
HP-PrPdSn	11.5 GPa	↗1100 °C/20 min, →1100 °C/5 min, ↓800 °C/1 min, ↘800 to 700 °C/60 min, ↓r. t.
HP-NdPdSn	11.5 GPa	↗1100 °C/20 min, →1100 °C/5 min, ↓800 °C/1 min, ↘800 to 700 °C/60 min, ↓r. t.

↗: increase of temperature in  $x$  min, →: constant temperature for  $x$  min, ↘: decrease of temperature in  $x$  min, ↓: quenching of the sample to room temperature.

Table 2. Lattice parameters of the normal- and high-pressure modifications of *RETSn* ( $RE = \text{La, Pr, Nd, Sm}$ ;  $T = \text{Ni, Pd}$ ).

Compound	$a$ (pm)	$b$ (pm)	$c$ (pm)	$V$ (nm <sup>3</sup> )	$V/Z$ (nm <sup>3</sup> )	Reference
NP-CeNiSn	753.7(3)	459.6(1)	761.5(2)	0.2638	0.0660	this work
	752.3(3)	459.2(2)	756.1(5)	0.2612	0.0653	[39]
HP-CeNiSn	744.6(2)	$a$	406.39(9)	0.1951	0.0650	this work
NP-PrNiSn	746.7(1)	457.28(8)	767.2(1)	0.2620	0.0655	this work
	744.2(7)	455.1(4)	766.1(6)	0.2595	0.0649	[39]
	744.0	456.0	770.6	0.2614	0.0654	[18]
HP-PrNiSn	743.4(2)	$a$	403.43(8)	0.1931	0.0644	this work
NP-NdNiSn	739.8(1)	454.2(1)	768.2(2)	0.2581	0.0645	this work
	730.5(6)	452.3(1)	774.0(5)	0.2557	0.0639	[39]
	732.5	451.5	772.5	0.2555	0.0639	[38]
HP-NdNiSn	741.6(3)	$a$	403.0(2)	0.1919	0.0640	this work
NP-SmNiSn	730.2(2)	450.8(1)	769.0(2)	0.2531	0.0633	this work
	727.7(2)	450.1(1)	767.5(3)	0.2514	0.0629	[39]
	730.4	450.9	768.0	0.2529	0.0632	[18]
	734.12(1)	$a$	397.66(1)	0.1856	0.0619	this work
NP-LaPdSn	763.9(1)	473.94(7)	799.7(1)	0.2895	0.0724	this work
	763.1	473.2	798.6	0.2884	0.0721	[40]
HP-LaPdSn	765.1(2)	$a$	419.3(1)	0.2126	0.0709	this work
NP-PrPdSn	748.7(3)	467.9(2)	795.9(3)	0.2788	0.0697	this work
	747.5	468.0	797.9	0.2791	0.0698	[38]
	752.3	467.9	796.6	0.2804	0.0701	[7]
	752.5(3)	466.9(2)	797.2(4)	0.2801	0.0700	[37]
	757.3(3)	$a$	414.0(2)	0.2056	0.0685	this work
NP-NdPdSn	742.8(2)	466.5(1)	795.3(2)	0.2756	0.0689	this work
	742.4	466.5	795.1	0.2754	0.0688	[18]
	747.3	465.4	794.1	0.2762	0.0690	[7]
	747.6(3)	466.6(2)	794.6(3)	0.2772	0.0693	[37]
HP-NdPdSn	756.3(2)	$a$	412.6(1)	0.2044	0.0681	this work

pressure/high-temperature experiments and investigations of some of the properties of compounds *RENiSn* ( $RE = \text{Ce, Pr, Nd, Sm}$ ) and *REPdSn* ( $RE = \text{La, Pr, Nd}$ ).

## Experimental Section

### Synthesis

Starting materials for the synthesis of the *RENiSn* and *REPdSn* stannides were ingots of the rare earth metals (Johnson-Matthey or smart elements), nickel wire ( $\varnothing$  0.38 mm, Johnson-Matthey), palladium powder (Degussa-Hüls, 200 mesh, > 99.9%), and tin granules (Merck), all with stated purities better than 99.9%. Pieces

of the rare earth ingots were first arc-melted [23] to small buttons under an argon atmosphere. The argon was purified before with molecular sieves, silica gel, and titanium sponge (900 K). Subsequently the rare earth buttons, pieces of the nickel wire or cold-pressed pellets ( $\varnothing$  6 mm) of palladium and pieces of the tin granules were arc-melted. The samples were remelted three times to ensure homogeneity. CeNiSn and the palladium containing stannides were obtained in X-ray pure form already after the arc-melting procedure. The *RENiSn* ( $RE = \text{Pr, Nd, Sm}$ ) buttons were sealed in evacuated silica tubes and annealed at 1070 K for three days. All polycrystalline samples are stable in air over weeks.

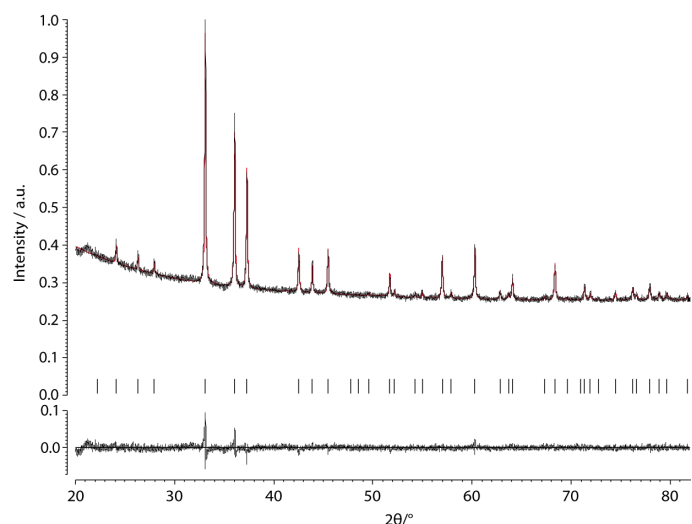


Fig. 1. Rietveld refinement plot for HP-SmNiSn. The observed intensities are indicated with open circles and the calculated pattern with a line on top of the circles. The vertical lines indicate the Bragg positions. The difference  $I_{\text{obs}} - I_{\text{calc}}$  is drawn below the Bragg indicators.

### High-pressure/high-temperature treatment

The high-pressure/high-temperature treatment took place via a multianvil assembly. Details about the technique and the construction of the different assemblies can be found in several references [24–27]. Boron nitride crucibles were loaded with carefully milled samples of NP-RENiSn or NP-REPdSn, compressed within several hours to a pressure of 7.5–11.5 GPa and then heated to temperatures between 1100 and 1200 °C. After holding the corresponding temperature for several minutes, the samples were quenched or cooled down to temperatures between 700 and 900 °C within a minute. Subsequent annealing under pressure at elevated temperatures for several hours enhanced the crystallinity of the samples followed by quenching to r.t. Table 1 gives a compilation of the exact synthesis conditions and temperature programs of the various high-pressure experiments. After decompression, the samples were carefully separated from the surrounding assembly parts.

The polycrystalline samples are silvery with metallic lustre. Powdered samples of both modifications are dark grey.

### EDX data

Semiquantitative EDX analyses on the crystals investigated on the diffractometer were carried out by use of a Leica 420i scanning electron microscope with the rare earth trifluorides, CeO<sub>2</sub>, nickel, palladium, and tin as standards. The experimentally observed compositions were close to the equiatomic ones. No impurity elements heavier than sodium (detection limit of the instrument) were found.

### X-Ray diffraction

The polycrystalline samples of the normal- and high-pressure phases were characterized through X-ray powder

Table 3. X-Ray powder data ( $\text{CuK}\alpha_1$ ,  $\lambda = 1.54051 \text{ \AA}$ ) and structure refinement for HP-SmNiSn ( $P62m$ ,  $Z = 3$ ).

Empirical formula	SmNiSn
Formula weight, g mol <sup>-1</sup>	327.76
<i>a</i> , pm	734.12(1)
<i>c</i> , pm	397.66(1)
<i>V</i> , nm <sup>3</sup>	0.1856
Calculated density, g cm <sup>-3</sup>	8.79
Absorption correction ( $\mu\text{R}$ )	1
<i>F</i> (000), e	420
Range in $2\theta$ , deg	20–82
Scan mode; step width, deg	$\omega/2\theta$ ; 0.005
No. data points	12383
Total no. Bragg reflections	37
No. structure parameters	7
No. total parameters	20
$R_F/R_{\text{wp}}$	0.039/0.017
$R_{\text{Bragg}}(I)$	0.013
Bérar-Lelann Factor	2.508

diffraction (Guinier technique, imaging plate detector, Fuji-film BAS-1800) using  $\text{CuK}\alpha_1$  radiation and  $\alpha$ -quartz ( $a = 491.30$  and  $c = 540.46$  pm) as an internal standard. The lattice parameters (Table 2) of all modifications were refined from the powder data by a least-squares routine. The proper indexing was ensured by intensity calculations [28].

X-Ray powder data for Rietveld refinement (Fig. 1 and Table 3) of HP-SmNiSn were collected in transmission geometry at r.t. on a Huber Guinier powder diffractometer (G670 Huber Diffraktionstechnik GmbH & Co. KG) with quartz-monochromatized  $\text{CuK}\alpha_1$  radiation ( $\lambda = 154.06$  pm) in the range  $20 \leq 2\theta \leq 82^\circ$ .

Single crystals of NP-CeNiSn, NP-NdNiSn, HP-PrNiSn, HP-LaPdSn, HP-PrPdSn, and HP-NdPdSn were selected from the samples by mechanical fragmentation, and their quality was checked by Laue photographs on a Buerger

Table 4. Crystal data and structure refinement for NP-CeNiSn, NP-NdNiSn and HP-PrNiSn at r. t.

Empirical formula	NP-CeNiSn	NP-NdNiSn	HP-PrNiSn
Space group; $Z$	$Pnma$ ; 4	$Pnma$ ; 4	$P\bar{6}2m$ ; 3
Molar mass, $\text{g mol}^{-1}$	317.52	321.64	318.31
Unit cell dimensions			
$a$ , pm	753.7(3)	739.8(1)	743.4(2)
$b$ , pm	459.6(1)	454.2(1)	$a$
$c$ , pm	761.5(2)	768.2(2)	403.43(8)
$V$ , $\text{nm}^3$	0.2638	0.2581	0.1930
Calculated density, $\text{g cm}^3$	8.00	8.28	8.21
Crystal size, $\mu\text{m}^3$	$20 \times 30 \times 50$	$20 \times 60 \times 80$	$40 \times 40 \times 90$
Detector distance, mm	60	–	–
Exposure time	5 min	–	–
$\omega$ range/increment, deg	0–180/1.0	–	–
Transm. ratio (max/min)	1.70	1.34	1.58
Absorption coefficient, $\text{mm}^{-1}$	33.0	19.1	18.5
$F(000)$ , e	544	552	411
$\theta$ range, deg	3–30	3–30	2–30
Range in $hkl$	–10/+9; –6/+5; $\pm 10$	$\pm 13$ ; $\pm 8$ ; $\pm 13$	$\pm 13$ ; $\pm 13$ ; $\pm 7$
Total no. reflections	2594	5730	5088
Independent reflections	430	828	458
$R_{\text{int}}$	0.102	0.054	0.041
Reflections with $I \geq 2\sigma(I)$	239	693	450
Data/parameters	430/20	828/20	458/14
Goodness-of-fit on $F^2$	0.489	1.058	1.142
Final indices $R_1/wR_2$ [ $I \geq 2\sigma(I)$ ]	0.022/0.030	0.023/0.039	0.010/0.021
Final indices $R_1/wR_2$ (all data)	0.073/0.037	0.033/0.041	0.011/0.022
Extinction coefficient	0.0035(2)	0.0039(4)	0.0082(7)
Flack parameter	–	–	0.00(3)
Largest diff. peak/hole, $\text{e \AA}^{-3}$	1.83/–1.46	1.42/–1.97	0.78/–0.75

camera using white Mo radiation. Intensity data of HP-PrNiSn and NP-NdNiSn were collected at r. t. by use of a four-circle diffractometer (CAD4) with graphite-monochromatized  $\text{AgK}\alpha$  radiation and a scintillation counter with pulse-height discrimination. The scans were taken in the  $\omega/2\theta$  mode, and empirical absorption corrections were applied on the basis of  $\psi$ -scan data, accompanied by spherical absorption corrections. Single crystals of NP-CeNiSn, HP-PrPdSn, and HP-NdPdSn were measured at r. t. by use of a Stoe IPDS-II imaging plate diffractometer in oscillation mode (graphite-monochromatized  $\text{MoK}\alpha$  radiation). Numerical absorption corrections were applied to the data sets. Data of the HP-LaPdSn crystal were collected on a Kappa CCD diffractometer (Bruker AXS/Nonius, Karlsruhe, Germany) equipped with a rotating anode and graphite-monochromatized  $\text{MoK}\alpha$  radiation ( $\lambda = 71.07$  pm). A multi-scan absorption correction was applied to this data set. All relevant details concerning the data collections and evaluations are listed in Tables 4 and 5.

#### Structure refinements

The isotopy of the normal-pressure modifications with the orthorhombic TiNiSi (space group  $Pnma$ ) [19] and of the high-pressure modifications with the hexagonal ZrNiAl type (space group  $P\bar{6}2m$ ) [22, and refs. therein] was already ev-

ident from the Guinier patterns, in agreement with previous investigations on the  $\text{REPtSn}$  series [11–13]. Results of careful evaluations of the data sets were compatible with these space groups, and the atomic parameters of NP- and HP-CePtSn [11] were taken as starting values. The structures were refined using SHELXL-97 [29] (full-matrix least-squares refinement on  $F^2$ ) with anisotropic displacement parameters for all atoms. As a check for possible mixed occupied sites, all occupancy parameters were refined in separate series of least-squares cycles. Because all sites were fully occupied within two standard deviations, the ideal occupancies were assumed again in the final refinement cycles. Refinement of the correct absolute structures of the hexagonal phases was ensured through calculation of the Flack parameter [30, 31]. The final difference Fourier syntheses were flat (Tables 4 and 5). The positional parameters and interatomic distances (exemplarily for NP-CeNiSn and HP-PrNiSn) are listed in Tables 6 and 7.

The HP-PrNiSn crystal showed slightly enhanced  $U_{22}$  and  $U_{33}$  parameters for the Pr and Ni2 positions, respectively. This anisotropy is a hint for superstructure formation (deformation of the rare earth prisms), similar to HfRhSn [32], ScPdSn [33], and ScPtSn [34]. Critical reinvestigation of the crystal on the image plate diffractometer, however, revealed no superstructure reflections, that would re-

Table 5. Crystal data and structure refinement for HP-LaPdSn, HP-PrPdSn and HP-NdPdSn at r. t.

Empirical formula	HP-LaPdSn	HP-PrPdSn	HP-NdPdSn
Space group; $Z$	$P\bar{6}2m$ ; 3	$P\bar{6}2m$ ; 3	$P\bar{6}2m$ ; 3
Molar mass, $\text{g mol}^{-1}$	364.00	366.00	369.33
Unit cell dimensions			
$a$ , pm	765.1(2)	757.3(3)	756.3(2)
$c$ , pm	419.3(1)	414.0(2)	412.6(1)
$V$ , $\text{nm}^3$	0.2126	0.2056	0.2044
Calculated density, $\text{g cm}^{-3}$	8.53	8.87	9.00
Crystal size, $\mu\text{m}^3$	$10 \times 10 \times 10$	$10 \times 20 \times 30$	$10 \times 20 \times 20$
Detector distance, mm	50	60	60
Exposure time, min	–	5	5
Scan time per degree, s	70	–	–
$\omega$ range/increment, deg	0–180/2.0	0–180/1.0	0–180/1.0
Transm. ratio (max/min)	–	1.63	1.44
Absorption coefficient, $\text{mm}^{-1}$	29.5	32.6	34.0
$F(000)$ , e	459	465	468
$\theta$ range, deg	4–38	3–33	3–35
Range in $hkl$	$\pm 13; \pm 10; \pm 7$	$\pm 11; -11/+7; \pm 6$	$\pm 10; \pm 12; \pm 6$
Total no. reflections	1482	2055	3073
Independent reflections	455	309	361
$R_{\text{int}}$	0.029	0.289	0.06
Reflections with $I \geq 2\sigma(I)$	416	125	321
Data / parameters	455 / 14	309 / 14	361 / 14
Goodness-of-fit on $F^2$	0.975	0.375	0.843
Final indices $R_1/wR_2$ [ $I \geq 2\sigma(I)$ ]	0.017/0.024	0.036/0.077	0.023/0.023
Final indices $R_1/wR_2$ (all data)	0.023/0.024	0.125/0.125	0.032/0.024
Extinction coefficient	0.0015(3)	0.0031(1)	0.0061(2)
Flack parameter	0.02(2)	0.07(17)	0.04(3)
Largest diff. peak/hole, $\text{e \AA}^{-3}$	1.42/–1.55	2.23/–1.96	1.49/–2.24

sult from the *klassengleiche* symmetry reduction from  $P\bar{6}2m$  to  $P\bar{6}2c$ .

Further details of the crystal structure investigations may be obtained from Fachinformationszentrum Karlsruhe, 76344 Eggenstein-Leopoldshafen, Germany (fax: +49-7247-808-666; e-mail: [crysdata@fiz-karlsruhe.de](mailto:crysdata@fiz-karlsruhe.de), [http://www.fiz-informationsdienste.de/en/DB/icsd/depot\\_anforderung.html](http://www.fiz-informationsdienste.de/en/DB/icsd/depot_anforderung.html)) on quoting the deposition numbers CSD-419194 (NP-CeNiSn), CSD-419192 (HP-PrNiSn), CSD-419195 (NP-NdNiSn), CSD-419190 (HP-LaPdSn), CSD-419193 (HP-PrPdSn), and CSD-419191 (HP-NdPdSn).

#### Physical property measurements

The magnetic and heat capacity measurements were carried out on a Quantum Design Physical Property Measurement System (PPMS) using *ac*-, *dc*-MS and heat capacity options, respectively. For *dc* measurements, HP-PrPdSn and HP-NdPdSn samples were packed in kapton foil and attached to the sample holder rod of a VSM for measuring the magnetic properties in the temperature range 3–305 K with magnetic flux densities up to 80 kOe. For *ac*-MS measurements HP-NdPdSn was enclosed in a thin-walled gelatin capsule. For heat capacity ( $C_P$ ) measurements (2.1–30 K) the samples were fixed to the platform of a precalibrated heat capacity puck using Apiezon N grease.

## Discussion

### Crystal chemistry

The series of RENiSn and REPdSn compounds with the early rare earth elements have been studied in high-pressure and high-temperature treatments. Similar to the REPtSn stannides reported recently [11–13], we

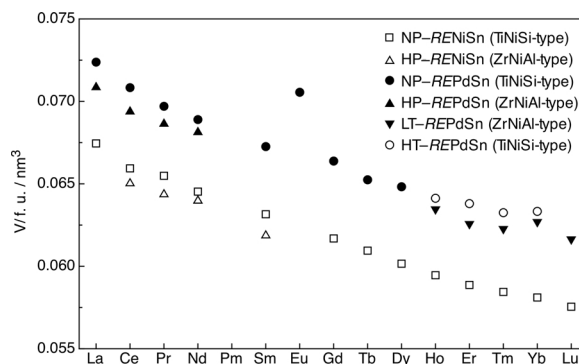


Fig. 2. Plot of the cell volumes of the orthorhombic normal- and hexagonal high-pressure modifications of RENiSn and REPdSn. For better comparison we plot the volumes per formula unit.

Table 6. Atomic coordinates and anisotropic displacement parameters ( $\text{pm}^2$ ) for NP-CeNiSn, NP-NdNiSn and HP-RETSn ( $RE = \text{La, Pr, Nd, Sm}$ ;  $T = \text{Ni, Pd}$ ).  $U_{\text{eq}}$  is defined as one third of the trace of the orthogonalized  $U_{ij}$  tensor. The anisotropic displacement factor exponent takes the form  $-2\pi^2[(ha^*)^2U_{11} + \dots + 2kha^*b^*U_{12}]$ .  $U_{23} = 0$ . The positional parameters of HP-SmNiSn were determined from a powder Rietveld refinement.

Atom	Wyck. pos.	$x$	$y$	$z$	$U_{11}$	$U_{22}$	$U_{33}$	$U_{12}$	$U_{13}$	$U_{\text{eq}}/U_{\text{iso}}$
<b>NP-CeNiSn</b>										
Ce	4c	0.01803(12)	1/4	0.69733(10)	31(4)	43(5)	62(4)	0	6(4)	46(2)
Ni	4c	0.3113(3)	1/4	0.4183(4)	125(10)	42(13)	75(11)	0	17(9)	80(5)
Sn	4c	0.18618(14)	1/4	0.0907(2)	51(5)	33(7)	47(5)	0	4(4)	44(3)
<b>NP-NdNiSn</b>										
Nd	4c	0.01531(3)	1/4	0.70001(3)	69(1)	82(1)	97(1)	0	2(1)	83(1)
Ni	4c	0.30615(9)	1/4	0.41613(8)	148(3)	90(2)	96(2)	0	3(2)	111(1)
Sn	4c	0.18789(4)	1/4	0.08825(4)	87(1)	65(1)	84(1)	0	1(1)	79(1)
<b>HP-PrNiSn</b>										
Pr	3f	0.59061(3)	0	0	83(1)	120(1)	69(1)	60(1)	0	86(4)
Ni1	1a	0	0	0	88(2)	$U_{11}$	62(3)	44(1)	0	79(1)
Ni2	2d	2/3	1/3	1/2	92(2)	$U_{11}$	224(4)	46(1)	0	136(1)
Sn	3g	0.25052(3)	0	1/2	68(1)	71(1)	70(1)	36(1)	0	69(1)
<b>HP-SmNiSn (Rietveld powder data)</b>										
Sm	3f	0.5924(2)	0	0	–	–	–	–	–	150(7)
Ni1	1a	0	0	0	–	–	–	–	–	45(32)
Ni2	2d	2/3	1/3	1/2	–	–	–	–	–	217(29)
Sn	3g	0.2520(4)	0	1/2	–	–	–	–	–	210(9)
<b>HP-LaPdSn</b>										
La	3f	0.58610(5)	0	0	91(1)	99(2)	86(1)	49(1)	0	91(1)
Pd1	1a	0	0	0	108(2)	$U_{11}$	78(3)	54(1)	0	98(1)
Pd2	2d	2/3	1/3	1/2	114(2)	$U_{11}$	118(2)	57(1)	0	116(1)
Sn	3g	0.24682(5)	0	1/2	88(1)	92(2)	88(2)	46(1)	0	89(1)
<b>HP-PrPdSn</b>										
Pr	3f	0.5890(4)	0	0	35(10)	39(14)	28(13)	20(7)	0	34(6)
Pd1	1a	0	0	0	23(18)	$U_{11}$	69(38)	11(9)	0	38(13)
Pd2	2d	2/3	1/3	1/2	33(13)	$U_{11}$	86(32)	17(7)	0	51(11)
Sn	3g	0.2513(4)	0	1/2	15(12)	43(17)	60(20)	21(9)	0	36(8)
<b>HP-NdPdSn</b>										
Nd	3f	0.58998(8)	0	0	65(2)	83(3)	64(2)	41(1)	0	69(1)
Pd1	1a	0	0	0	74(4)	$U_{11}$	54(6)	37(2)	0	67(3)
Pd2	2d	2/3	1/3	1/2	73(3)	$U_{11}$	98(5)	37(1)	0	82(2)
Sn	3g	0.25187(8)	0	1/2	62(3)	62(3)	62(3)	31(2)	0	62(1)

observe a pressure-induced phase transition from the orthorhombic TiNiSi [19] to the hexagonal ZrNiAl [22, and refs. therein] type. In all cases, the cell volume per formula unit (Fig. 2) is smaller for the high-pressure phases.

With respect to the physical properties, CeNiSn is the most popular compound in the family of RENiSn stannides. So far 219 entries occur in the current SciFinder Scholar version [35]. CeNiSn is interesting, because it is an anomalous valence-fluctuating compound having no magnetic order but instead a *pseudo*-energy gap at the Fermi level. Therefore, it was highly desirable to investigate the high-pressure modification. However, we obtained CeNiSn only as a two-phase sample with NP-CeNiSn and HP-CeNiSn in almost

equal amounts. At the most extreme HP/HT conditions CeNiSn decomposes mainly into CeNi<sub>2</sub>Sn<sub>2</sub>. The cell volume of HP-CeNiSn (Table 2) is smaller than that of NP-CeNiSn, and we can thus expect predominantly tetravalent cerium for the high-pressure modification.

The CeNiSn structure had been refined in the non-centrosymmetric space group  $Pna2_1$  [36]. However, our present single crystal data clearly prove that there is no violation of the mirror planes at  $y = 1/4$  and  $y = 3/4$ , and that the centrosymmetric description is adequate, similar to CePdSn [14] and CePtSn [11].

Due to the reconstructive phase transition from the TiNiSi to the ZrNiAl type, the near-neighbor coordination of the rare earth atoms changes drastically. As an example, we present the cerium and neodymium co-

Table 7. Interatomic distances (pm), calculated with the powder lattice parameters in NP-CeNiSn and HP-PrNiSn. All distances of the first coordination spheres are listed. Standard deviations are all equal or smaller than 0.3 pm.

NP-CeNiSn				HP-PrNiSn			
Ce:	1	Ni	306.6	Pr:	4	Ni2	302.1
	2	Ni	312.5		1	Ni1	304.3
	2	Sn	320.2		2	Sn	323.4
	1	Sn	325.3		4	Sn	333.6
	2	Sn	330.3		4	Pr	389.6
	1	Ni	331.6		2	Pr	403.4
	1	Sn	332.7				
	2	Ni	349.5				
	2	Ce	379.3				
	2	Ce	385.3				
Ni:	2	Sn	264.7	Ni1:	6	Sn	274.5
	1	Sn	266.7		3	Pr	304.3
	1	Sn	282.6	Ni2:	3	Sn	283.6
	1	Ce	306.6		6	Pr	302.1
	2	Ce	312.5				
	1	Ce	331.6				
	2	Ce	349.5				
	Sn:	2	Ni	264.7	Sn:	2	Ni1
1		Ni	266.7	2		Ni2	283.6
1		Ni	282.6	2	Sn	322.6	
2		Ce	320.2	2	Pr	323.4	
1		Ce	325.3	4	Pr	333.6	
2		Ce	330.3				
1		Ce	332.7				

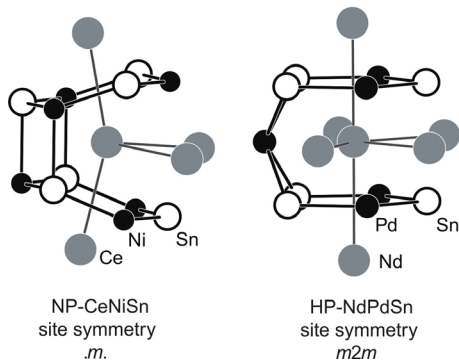


Fig. 3. Near-neighbor coordination of the rare earth atoms in NP-CeNiSn and HP-NdPdSn. Rare earth, transition metal and tin atoms are drawn as medium grey, black filled, and open circles, respectively.

ordinations in NP-CeNiSn and HP-NdPdSn in Fig. 3. This change in near-neighbor coordination (different  $RE-RE$  and  $RE-T$  distances) is responsible for the different magnetic behavior of the NP- and HP-phases. The crystal chemical peculiarities of the  $RENiSn$  and  $REPdSn$  stannides discussed herein are similar to those of the  $REPtSn$  series. For further details, additional drawings, and an evaluation of chemical bonding, we refer to our previous work [11–13].

### Physical properties of HP-PrPdSn and HP-NdPdSn

#### HP-PrPdSn

The magnetic behavior of NP-PrPdSn had been studied on polycrystalline samples [7, 37, 41]. Sakurai *et al.* reported a Néel temperature for NP-PrPdSn of  $T_N = 3.5$  K [41]. More detailed studies by Zygmunt *et al.* showed that NP-PrPdSn orders antiferromagnetically at  $T_N = 4.3$  K [37]. In Fig. 4, we present the dc ( $\chi$ ) and  $\chi^{-1}(T)$  values of HP-PrPdSn measured in an applied dc field of 10 kOe. The susceptibility  $\chi(T)$  increases monotonously with decreasing temperature, as expected for a paramagnet. HP-PrPdSn shows Curie-Weiss behavior. Fitting of the experimental data in the temperature region 50–300 K revealed an effective magnetic moment of  $\mu_{\text{eff}} = 3.61(1) \mu_B/\text{Pr}$  atom and a Weiss constant  $\theta_p = -8.9(5)$  K. The observed value is close to the value of  $3.58 \mu_B$  expected for a free  $\text{Pr}^{3+}$  ion. The negative value of  $\theta_p$  indicates antiferromagnetic interactions. NP-PrPdSn showed comparable values for  $\mu_{\text{eff}}$  and  $\theta_p$  [7, 37]. The dc  $\chi(T)$  measurement of HP-PrPdSn at 10 kOe gave no hint for magnetic ordering. An anomaly at around 3 K is clearly visible in the  $\chi(T)$  curve measured at low field of 100 Oe (Fig. 5). The  $\chi(T)$  data measured in ZFC and FC state of the sample do not bifurcate and are the same within the experimental errors. To probe any response of this anomaly to the dc field, we have measured  $\chi(T)$  of HP-PrPdSn at different applied fields and plotted these data in Fig. 6. This Figure clearly shows the field dependence of the susceptibility. The moment values decrease with increasing field. The drop in  $\chi(T)$ , ob-

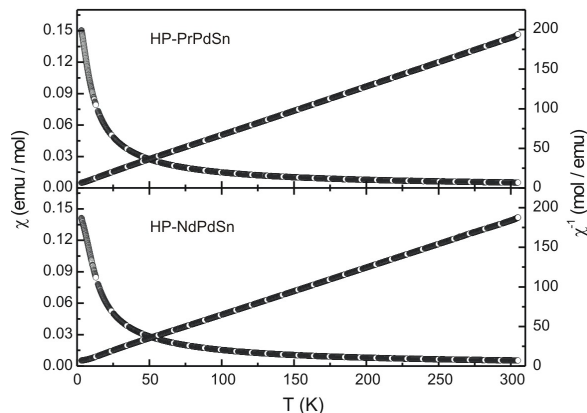


Fig. 4. Temperature dependence of the magnetic susceptibility ( $\chi(T)$  and  $\chi^{-1}(T)$ ) of HP-PrPdSn and HP-NdPdSn measured at a magnetic flux density of 1 T.

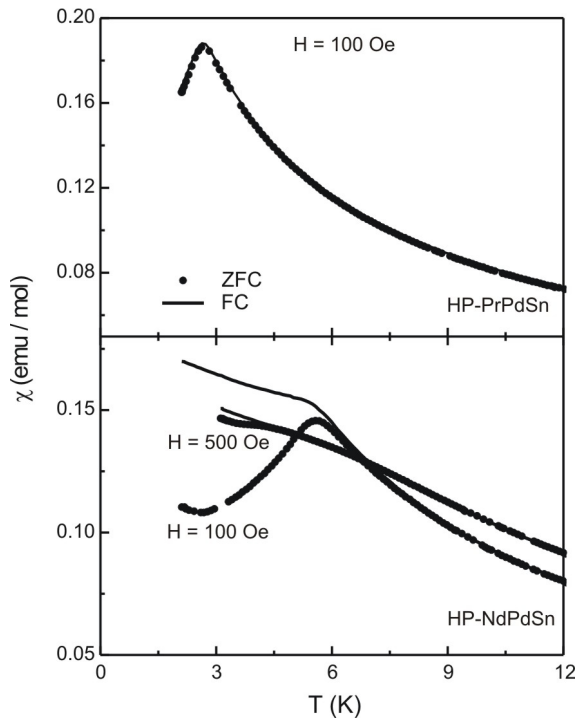


Fig. 5. Susceptibility  $\chi$  vs.  $T$  measured in ZFC and FC conditions in fields of 100 and 500 Oe for HP-PrPdSn and HP-NdPdSn.

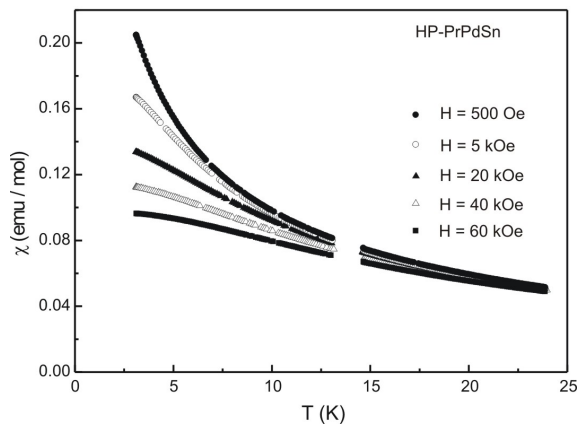


Fig. 6. The *dc* susceptibility of HP-PrPdSn measured in ZFC state of the sample at several applied fields.

served at 100 Oe, also vanishes with increasing field. The overlap of the ZFC-FC curves rules out any spin-glass anomalies. Therefore, the origin of the anomaly can be due to short range magnetic ordering arising due to inhomogeneous magnetism (see below).

The magnetization in the ZFC state of HP-PrPdSn (Fig. 7) varies in an almost linear fashion at 20

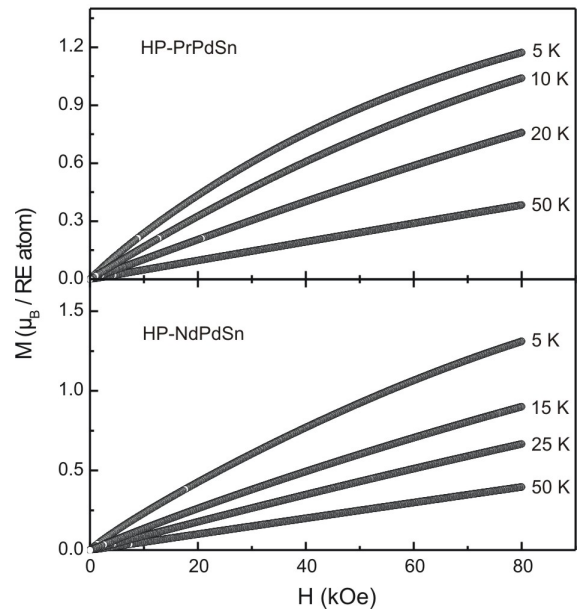


Fig. 7. Magnetization isotherms of HP-PrPdSn and HP-NdPdSn at various temperatures.

and 50 K as expected for a paramagnetic material. At 5 and 10 K the curvature becomes more pronounced, the isotherms increase non-linearly with increasing  $H$ , the sample thus behaving as an antiferromagnet without saturation up to 80 kOe. The moment value at 80 kOe and 5 K is  $1.17 \mu_B/\text{Pr atom}$ , *ca.* 37 % of the maximum possible value of  $g_J \times J = 3.20 \mu_B$  for  $\text{Pr}^{3+}$ . Such reduced magnetization values often occur in intermetallic praseodymium compounds and can be attributed to crystal field splitting of the  $J = 4$  ground state of  $\text{Pr}^{3+}$  and have also been observed for other equiatomic praseodymium intermetallics, *e. g.* PrRhSn [42] and PrRhZn [43].

In Fig. 8 the specific heat ( $C_P$ ) data are plotted for HP-PrPdSn. The anomalies observed in the magnetic measurements can also be seen for  $C_P$  in the form of a broad peak around 5 K. The absence of any clear peak is indicative of inhomogeneous magnetism in HP-PrPdSn. Thus, the  $C_P$  data are in line with the susceptibility data. In the low temperature region, above the broad peak, the specific heat is of the form  $C_P = \gamma T + \beta T^3$ , where  $\gamma$  is the electronic contribution and  $\beta$  is the lattice contribution. The Debye temperature,  $\Theta_D$ , can be estimated from the equation  $\beta = (12\pi^4 n k_B) / (5\Theta_D^3)$ , where  $k_B$  is the Boltzmann constant and  $n$  is the number of atoms per formula unit. From the plot of  $C_P/T$  vs.  $T^2$  in the temperature

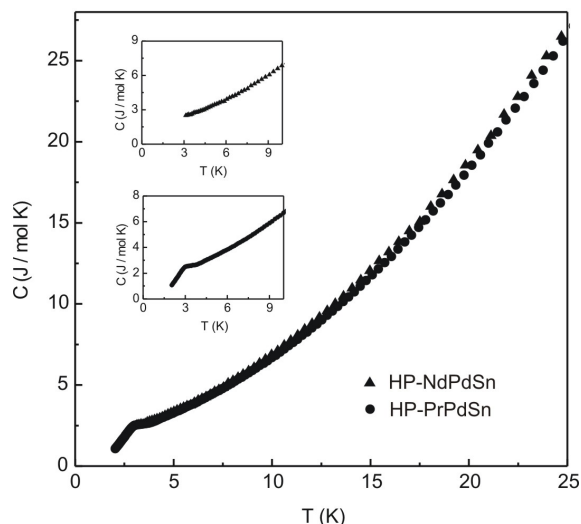


Fig. 8. Heat capacity  $C_p$  vs.  $T$  for HP-PrPdSn and HP-NdPdSn. The insets highlight the features below 10 K.

range 7–16 K we find  $\gamma = 585 \text{ mJ K}^{-2} \text{ mol}^{-1}$ ,  $\beta = 0.86 \text{ mJ K}^{-4} \text{ mol}^{-1}$ , and  $\Theta_D = 189 \text{ K}$ .

#### HP-NdPdSn

The magnetic behavior of NP-NdPdSn had been studied on polycrystalline samples [7, 37, 41]. Zygumunt *et al.* reported that NP-NdPdSn orders antiferromagnetically at  $T_N = 2.4 \text{ K}$  and shows Curie-Weiss behavior with an effective magnetic moment of  $3.68 \mu_B/\text{Nd atom}$  and a Weiss constant  $\theta_p = -11 \text{ K}$  [37], while Sakurai *et al.* reported a Néel temperature of  $3.2 \text{ K}$  [41]. However, Adroja *et al.* found a magnetic moment of  $4.93 \mu_B/\text{Nd atom}$  and  $\theta_p = -8 \text{ K}$  [7]. This value is much higher than the value expected for a free  $\text{Nd}^{3+}$  ion.

The *dc* susceptibility for HP-NdPdSn measured at 10 kOe in ZFC state is shown in Fig. 4.  $\chi$  exhibits an upturn below 50 K, with no peak at lower temperatures. The inverse susceptibility follows Curie-Weiss behavior above 50 K. From the Curie-Weiss fit of the linear region,  $\theta_p$  and  $\mu_{\text{eff}}$  for HP-NdPdSn are  $-8.6(1) \text{ K}$  and  $3.66(1) \mu_B/\text{Nd atom}$ , respectively. The  $\mu_{\text{eff}}$  value obtained experimentally is in close agreement with the value for the free  $\text{Nd}^{3+}$  ion ( $3.62 \mu_B$ ). The negative sign of  $\theta_p$  indicates that the interaction is of antiferromagnetic type.

The ZFC-FC curves for  $\chi(T)$  measured in  $H = 100$  and  $500 \text{ Oe}$  are shown in Fig. 5. For  $\chi(T)$  measured in low field of  $100 \text{ Oe}$ , we see a prominent peak

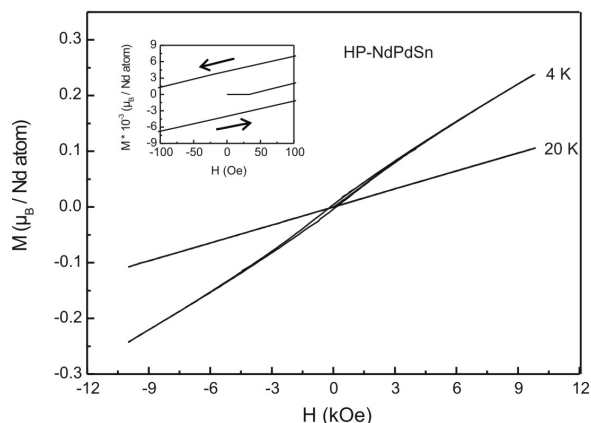


Fig. 9.  $M$  vs.  $H$  measured in a sweeping field of  $\pm 10 \text{ kOe}$  at 4 and 20 K for HP-NdPdSn. The low field hysteresis observed for  $T = 4 \text{ K}$  is shown in an expanded scale in the inset.

around  $5.8 \text{ K}$  in the ZFC measurement. The FC curve bifurcates from ZFC at this point, and increases at lower temperatures. This is a typical feature of spin glasses. We refer to this temperature as  $T_f$  or freezing temperature of spin glasses [44]. However, the peak smears out with application of higher magnetic fields, which is evident from the measurement with an applied field of  $500 \text{ Oe}$ . A freezing temperature is not seen in the ZFC-FC curves for the  $\chi(T)$  measured in  $1 \text{ kOe}$  field (measurement is not shown here), as this field strength is large enough to entirely smear out the peak.

The magnetizations as a function of the applied magnetic field at different temperatures spanning  $T_f$  of HP-NdPdSn are shown in Fig. 7. The magnetization for  $T = 25$  and  $50 \text{ K}$  increases linearly, as expected for a paramagnetic material. No traces of any ferromagnetic impurity or interactions could be observed. The  $M(H)$  at  $5 \text{ K}$  ( $T < T_f$ ) increases with increasing field with a tendency to saturate at higher fields. The value of magnetization at  $80 \text{ kOe}$  and  $5 \text{ K}$  is about  $1.3 \mu_B/\text{Nd atom}$ , corresponding to 40 % of the moment for the free  $\text{Nd}^{3+}$  ion. In order to probe these features, we have also measured low field hysteresis in field ramping up to  $\pm 10 \text{ kOe}$ . The  $M(H)$  loops are shown in Fig. 9. The sample was cooled to  $T < T_f$  in zero field state, and then the field was swept slowly. A small hysteresis could be seen at low fields ( $< 3 \text{ kOe}$ ,  $4 \text{ K}$ ) while sweeping the field in positive and negative directions. At  $20 \text{ K}$  (*i. e.*,  $T > T_f$ ) there is no such effect. These signatures of a spin glass are an interesting observation considering the fact that HP-NdPdSn is stoichiometric,

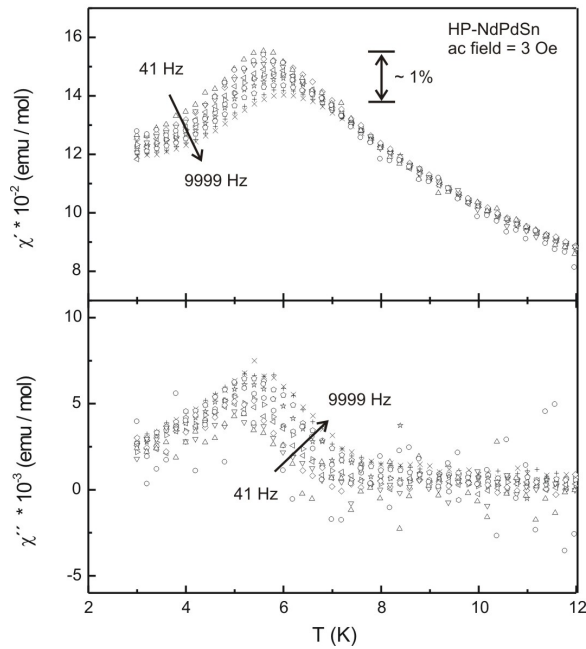


Fig. 10. Real ( $\chi'$ ) and imaginary ( $\chi''$ ) part of *ac* susceptibility for HP-NdPdSn measured in an *ac* field of 3 Oe, as a function of temperature for  $\nu = 41, 61, 111, 197, 341, 607, 1057, 1847, 3247, 5697$  and 9999 Hz.

and the spin glass anomalies arise presumably due to geometrical frustration (triangular arrangement of the neodymium atoms) as frequently observed in ZrNiAl type intermetallics [45]. Similar behavior was found in the system NP-NdPtSn *vs.* HP-NdPtSn [12].

The frequency dependence of *ac*  $\chi$  for HP-NdPdSn is shown in Fig. 10. For  $\nu = 41$  Hz, a broad peak around 5.6 K is seen, which shifts to higher temperatures with increasing frequency. The shift in temperature, though broadened, can be clearly seen when moving from  $\nu = 41$  Hz to 9999 Hz. As observed in metallic spin glasses, the peak height decreases while moving to higher temperatures with increasing frequency. The maximum observed for  $\nu = 41$  Hz shifts down by about 1 % for  $\nu = 9999$  Hz. Spin glasses exhibit a sudden onset in  $\chi''$  near  $T_f$ . HP-NdPdSn also exhibits a peak in  $\chi''$  around  $T_f$ . The appearance of a peak in  $\chi''$  (absorption) means that the relaxation processes are affecting the behavior, and by decoupling the spins from the lattice they cause the absorption [44]. Also the ratio of the change in peak temperature in  $\chi'$  to the change of the frequency given by  $(\Delta T_f / T_f) \Delta(\ln \nu)$  is observed to be of the order of 0.01, comparable to ideal spin glasses [46, 47].

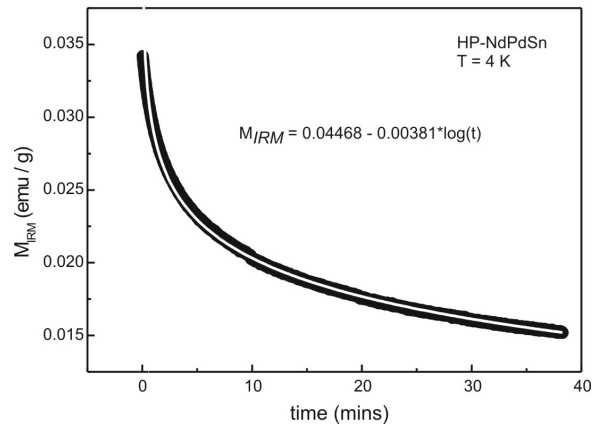


Fig. 11. Isothermal relaxation of magnetization measured as a function of time (in minutes) for HP-NdPdSn at  $T = 4$  K after subjecting the sample to a steady field of 5 kOe for five minutes (for details of the measurements, see text). The white line presents the logarithmic fit of the data.

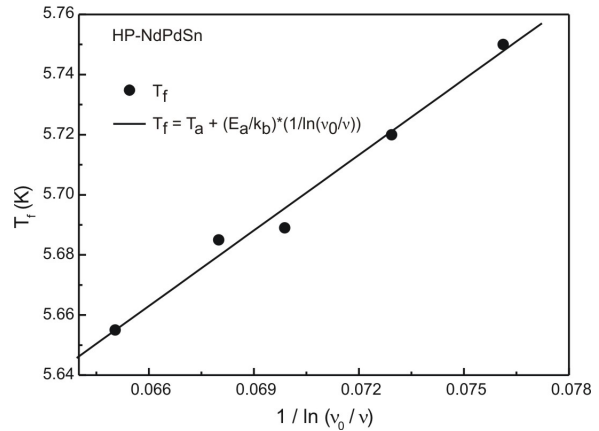


Fig. 12. Vogel-Fulcher law fit for HP-NdPdSn. For details see text.

The magnetization of a spin glass in a frozen state reacts to the externally applied field over a period of time. Therefore, in order to verify the spin-glass behavior for HP-NdPdSn exhibited in *ac*  $\chi$  and magnetization measurements, we measured the isothermal relaxation magnetization ( $M_{IRM}$ ) at 4 K. After zero field cooling of the sample a field of 5 kOe was applied for five minutes and then reduced to zero. For a period of 2400 seconds the  $M_{IRM}$  was measured as soon as the field reached zero (Fig. 11). The  $M_{IRM}$  decays logarithmically over the entire duration of the measurement and can be fitted to a function of the type  $M_{IRM} = P1 - P2 \log(t)$  where  $P1 = 0.04468$  and  $P2 = 0.00381$  are two fitting parameters, which depend upon the tem-

perature, waiting time and relaxation rate in ‘dynamical equilibrium’, similar to HP-NdPtSn [12].

The spin-glass behavior of HP-NdPdSn can be better understood by analyzing the *ac*  $\chi$  in greater detail. The shift of  $T_f$  with frequency can be understood by the Vogel-Fulcher (V-F) law given by

$$\nu = \nu_0 \exp \left[ \frac{-E_a}{k_B(T_f - T_a)} \right]$$

where  $\nu$  is the driving frequency,  $\nu_0$  is the characteristic spin glass frequency ( $\sim 10^8$  Hz for ideal spin glasses),  $E_a$  is the activation energy and  $T_a$  is called the ideal spin-glass temperature, which gives the strength of interaction among the clusters [44, 46]. Therefore, for a spin-glass system the plot of  $T_f$  vs.  $1/\ln(\nu_0/\nu)$  should be a straight line. Fig. 12 shows the V-F law fitting to the observed data, which establishes that HP-NdPdSn is indeed a spin-glass system. From the linear fit, we can deduce the values of  $T_a = 5.1$  K and  $E_a/k_B = 8.38$ .

Focusing on the  $C_p(T)$  of HP-NdPdSn in Fig. 5, the  $C_p$  data give no hint of magnetic ordering. Normally, spin glasses show a broad feature around  $T_f$  which smears out with application of a magnetic field. This was not observed in the case of HP-NdPdSn and can be due to a hardly stressed electronic system. From the linear fit of the plot  $C_p/T$  vs.  $T^2$  in the low-temperature region (between 7–16 K), we find the values:  $\gamma = 598$  mJ K<sup>-2</sup> mol<sup>-1</sup>,  $\beta = 0.90$  mJ K<sup>-4</sup> mol<sup>-1</sup> and  $\Theta_D = 186$  K. However, the *dc* and *ac* susceptibility results verify the spin-glass features in the HP-NdPdSn system.

#### Acknowledgements

This work was financially supported by the Deutsche Forschungsgemeinschaft. W.H. is grateful to the Stiftung Stipendienfonds of VCI for a PhD stipend. Special thanks go to Dr. P. Mayer and S. Albrecht (LMU München) for collecting the single-crystal X-ray diffraction data at the Kappa CCD diffractometer. H.H. is indebted to the Fonds der Chemischen Industrie for financial support.

- 
- [1] M. L. Fornasini, F. Merlo, *J. Alloys Compd.* **1995**, 219, 63.
- [2] E. Parthé, L. Gelato, B. Chabot, M. Penzo, K. Cen-zual, R. Gladyshevskii, *TYPIX–Standardized Data and Crystal Chemical Characterization of Inorganic Structure Types. Gmelin Handbook of Inorganic and Organometallic Chemistry* (8<sup>th</sup> edition), Springer, Berlin **1993**.
- [3] P. Villars, L. D. Calvert, *Pearson’s Handbook of Crystallographic Data for Intermetallic Phases* (2<sup>nd</sup> Edition), American Society for Metals, Materials Park, OH **1991**, and desk edition **1997**.
- [4] R.-D. Hoffmann, R. Pöttgen, *Z. Kristallogr.* **2001**, 216, 127.
- [5] A. E. Dwight, *Proc. Rare Earth Res. Conf.* **1976**, 1, 480.
- [6] K. Łatka, E. A. Görlich, R. Kmiec, R. Kruk, A. W. Pacyna, W. Chajec, *Mol. Phys. Rep.* **1998**, 22, 87.
- [7] D. T. Adroja, S. K. Malik, *Phys. Rev. B* **1992**, 45, 779.
- [8] C. P. Sebastian, G. Heymann, B. Heying, U. Ch. Rodewald, H. Huppertz, R. Pöttgen, *Z. Anorg. Allg. Chem.* **2007**, 633, 1551.
- [9] B. Heying, U. Ch. Rodewald, G. Heymann, W. Hermes, F. M. Schappacher, J. F. Riecken, C. P. Sebastian, H. Huppertz, R. Pöttgen, *Z. Naturforsch.* **2008**, 63b, 193.
- [10] A. Griбанov, A. Tursina, E. Murashova, Y. Seropegin, E. Bauer, H. Kaldarar, R. Lackner, H. Michor, E. Roy-anian, M. Reissner, P. Rogl, *J. Phys.: Condens. Matter* **2006**, 18, 9593.
- [11] J. F. Riecken, G. Heymann, T. Soltner, R.-D. Hoffmann, H. Huppertz, D. Johrendt, R. Pöttgen, *Z. Naturforsch.* **2005**, 60b, 821.
- [12] G. Heymann, S. Rayaprol, J. F. Riecken, R.-D. Hoffmann, U. Ch. Rodewald, H. Huppertz, R. Pöttgen, *Solid State Sci.* **2006**, 8, 1258.
- [13] J. F. Riecken, U. Ch. Rodewald, G. Heymann, S. Rayaprol, H. Huppertz, R.-D. Hoffmann, R. Pöttgen, *Z. Naturforsch.* **2006**, 61b, 1477.
- [14] G. Heymann, J. F. Riecken, S. Rayaprol, S. Christian, R. Pöttgen, H. Huppertz, *Z. Anorg. Allg. Chem.* **2007**, 633, 77.
- [15] C. P. Sebastian, G. Heymann, B. Heying, U. Ch. Rodewald, H. Huppertz, R. Pöttgen, *Z. Anorg. Allg. Chem.* **2007**, 633, 1551.
- [16] D. T. Adroja, S. K. Malik, B. D. Padalia, R. Vijayaraghavan, *Solid State Comm.* **1988**, 66, 1201.
- [17] E.-W. Scheidt, J. F. Riecken, G. Heymann, W. Scherer, H. Huppertz, R. Pöttgen, unpublished results.
- [18] A. E. Dwight, *J. Less-Common Met.* **1983**, 93, 411.
- [19] C. B. Shoemaker, D. P. Shoemaker, *Acta Crystallogr.* **1965**, 18, 900.
- [20] D. Kußmann, R. Pöttgen, B. Künnen, R. Müllmann, B. D. Mosel, G. Kotzyba, *Z. Kristallogr.* **1998**, 613, 356.
- [21] T. Görlach, S. Putselyk, A. Hamann, T. Tomanić, M. Uhlarz, F. M. Schappacher, R. Pöttgen, H. v. Löhneysen, *Phys. Rev. B* **2007**, 76, 205112.
- [22] M. F. Zumdick, R.-D. Hoffmann, R. Pöttgen, *Z. Naturforsch.* **1999**, 54b, 45.

- [23] R. Pöttgen, Th. Gulden, A. Simon, *GIT Labor-Fachzeitschrift* **1999**, 43, 133.
- [24] H. Huppertz, *Z. Kristallogr.* **2004**, 219, 330.
- [25] D. Walker, M. A. Carpenter, C. M. Hitch, *Am. Mineral.* **1990**, 75, 1020.
- [26] D. Walker, *Am. Mineral.* **1991**, 76, 1092.
- [27] D. C. Rubie, *Phase Trans.* **1999**, 68, 431.
- [28] K. Yvon, W. Jeitschko, E. Parthé, *J. Appl. Crystallogr.* **1977**, 10, 73.
- [29] G. M. Sheldrick, SHELXL-97, Program for the Refinement of Crystal Structures, University of Göttingen, Göttingen (Germany) **1997**.
- [30] H. D. Flack, G. Bernadinelli, *Acta Crystallogr.* **1999**, A55, 908.
- [31] H. D. Flack, G. Bernadinelli, *J. Appl. Crystallogr.* **2000**, 33, 1143.
- [32] M. F. Zumdick, R. Pöttgen, *Z. Kristallogr.* **1999**, 214, 90.
- [33] R. Mishra, R. Pöttgen, R.-D. Hoffmann, H. Trill, B. D. Mosel, H. Piotrowski, M. F. Zumdick, *Z. Naturforsch.* **2001**, 56b, 589.
- [34] T. Harmening, C. P. Sebastian, L. Zhang, C. Fehse, H. Eckert, R. Pöttgen, *Solid State Sci.* **2008**, 10, in press.
- [35] For the formula CeNiSn 219 entries occur in the SciFinder Scholar (version 2008): <http://www.cas.org/SCIFINDER/SCHOLAR/>
- [36] I. Higashi, K. Kobayashi, T. Takabatake, M. Kasaya, *J. Alloys Compd.* **1993**, 193, 300.
- [37] A. Zygmunt, A. Szytuła, *J. Alloys Compd.* **1995**, 219, 185.
- [38] D. Rossi, R. Marazza, R. Ferro, *J. Less-Common Met.* **1985**, 107, 99.
- [39] R. V. Skolozdra, O. É. Koretskaya, Yu. K. Gorelenko, *Inorg. Mater.* **1984**, 20, 520.
- [40] F. Canepa, S. Cirafici, *J. Alloys Compd.* **1996**, 232, 71.
- [41] J. Sakurai, Y. Yamaguchi, K. Mibu, T. Shinjo, *J. Magn. Mater.* **1990**, 84, 157.
- [42] K. Łątka, R. Kmieć, J. Gugrul, M. Rams, A. W. Pacyna, T. Schmidt, R. Pöttgen, *J. Solid State Chem.* **2005**, 178, 3101.
- [43] W. Hermes, A. F. Al Alam, S. F. Matar, R. Pöttgen, *Solid State Sci.* **2008**, in press.
- [44] J. A. Mydosh, *Spin Glasses: An Experimental Introduction*, Taylor & Francis, London **1993**.
- [45] A. Szytuła, *Crystal Structures and Magnetic Properties of RTX Rare Earth Intermetallics*, Wydawnictwo Uniwersytetu Jagiellońskiego, Kraków **1998**.
- [46] K. Binder, A. P. Young, *Rev. Mod. Phys.* **1986**, 58, 801.
- [47] C. A. M. Mulder, A. J. van Duynveldt, J. A. Mydosh, *Phys. Rev. B* **1981**, 23, 1384.